






# Characterizing the Advective Hot Flows of Nova-like Cataclysmic Variables in the X-Rays: The Case of BZ Cam and V592 Cas

Sölen Balman<sup>1,2,6</sup> , Eric M. Schlegel<sup>3</sup> , and Patrick Godon<sup>4,5</sup> <sup>1</sup> Department of Astronomy and Space Sciences, Faculty of Science, Istanbul University, Beyazit, 34119, Istanbul, Turkey; [solen.balman@gmail.com](mailto:solen.balman@gmail.com), [solen.balman@istanbul.edu.tr](mailto:solen.balman@istanbul.edu.tr)<sup>2</sup> Kadir Has University, Faculty of Engineering and Natural Sciences, Cibali 34083, Istanbul, Turkey<sup>3</sup> Department of Physics and Astronomy, University of Texas-San Antonio, San Antonio, TX 78249, USA<sup>4</sup> Department of Astrophysics & Planetary Science, Villanova University, 800 Lancaster Avenue, Villanova, PA 19085, USA<sup>5</sup> Henry A. Rowland Department of Physics & Astronomy, Johns Hopkins University, Baltimore, MD 21218, USA

Received 2021 December 17; revised 2022 April 5; accepted 2022 April 8; published 2022 June 13

## Abstract

We present a joint spectral analysis of ROSAT PSPC, Swift X-ray Telescope, and Nuclear Spectroscopic Telescope Array Focal Plane Module A/B (FPMA/B) data of the nova-like (NL) cataclysmic variables (CVs) BZ Cam and V592 Cas in the 0.1–78.0 keV band. Plasma models of collisional equilibrium fail to model the 6.0–7.0 iron line complex and continuum with  $\chi^2_\nu$  larger than 2.0. Our results show nonequilibrium ionization (NEI) conditions in the X-ray plasma with temperatures of 8.2–9.4 keV and 10.0–12.9 keV for BZ Cam and V592 Cas, respectively. The centroids of He-like and H-like iron ionization lines are not at their equilibrium values as expected from NEI conditions. We find power-law spectral components that reveal the existence of scattering and Comptonization with a photon index of 1.50–1.87. We detect a P Cygni profile in the H-like iron line of BZ Cam translating to outflows of 4500–8700 km s<sup>-1</sup> consistent with the fast winds in the optical and UV. This is the first time such a fast collimated outflow is detected in the X-rays from an accreting CV. An iron K $\alpha$  line around 6.2–6.5 keV is found revealing the existence of reflection effects in both sources. We study the broadband noise and find that the optically thick disk truncates in BZ Cam and V592 Cas consistent with transition to an advective hot flow structure. V592 Cas also exhibits a quasiperiodic oscillation at 1.4<sup>+2.6</sup><sub>-0.3</sub> mHz. In general, we find that the two NLs portray spectral and noise characteristics as expected from advective hot accretion flows at low radiative efficiency.

*Unified Astronomy Thesaurus concepts:* [Accretion \(14\)](#); [White dwarf stars \(1799\)](#); [Stellar accretion disks \(1579\)](#); [Spectroscopy \(1558\)](#); [Plasma astrophysics \(1261\)](#); [Nonthermal radiation sources \(1119\)](#); [X-ray binary stars \(1811\)](#); [X-ray astronomy \(1810\)](#); [X-ray sources \(1822\)](#); [Cataclysmic variable stars \(203\)](#); [Nova-like variable stars \(1126\)](#); [Stellar winds \(1636\)](#)

## 1. Introduction

Cataclysmic variables (CVs) are close binary systems where a white dwarf (WD) accretes matter from a late-type Roche-lobe-filling main-sequence star (Warner 1995). In nonmagnetic CVs the transferred material forms an accretion disk that reaches the WD. Standard accretion disk theory (Shakura & Sunyaev 1973) predicts half of the accretion luminosity to emerge from the disk and the other half from the boundary layer (BL) very close to the WD (Lynden-Bell & Pringle 1974). In the standard disk accretion model, the BL emission is such that during low mass accretion states it is optically thin emitting in the hard X-rays (Narayan & Popham 1993; Popham 1999) and for high accretion rate states ( $\dot{M}_{\text{acc}} \geq 10^{-(9-9.5)} M_{\odot}$ ), it is optically thick emitting in the soft X-rays and EUV (kT  $\sim$  10<sup>(5-5.6)</sup> K; Popham & Narayan 1995; Godon et al. 1995; Suleimanov et al. 2014; Hertfelder & Kley 2015, 2017). Narayan & Popham (1993) showed that optically thin BLs can be radially extended, advecting part of the accretion energy to the WD as a result of their inability to cool. The standard disk is

often found inadequate to model disk-dominated, high-state CVs (i.e., nova-likes) as well as several quiescent dwarf nova (e.g., eclipsing) in the optical and UV. In high-state systems, the standard disk spectrum is bluer than the observed UV spectra indicating that the expected hot optically thick inner flow of the BL is nonexistent (Puebla et al. 2007; Linnell et al. 2010). As a result, standard disk models with truncated inner disks have been calculated (e.g., Godon et al. 2017) and have been successfully fitted to the UV spectra while modeling the cooler disk. In addition, an improved model produced for a particular NL fits the FUV spectral slope and its features well, indicating that not much of a vertical structure of temperature exists and most dissipation occurs from the heated surface layers instead of the midplane of the disk (Hubeny & Long 2021). In general, UV analyses find extended emission above the disk supporting nonstandard accretion flows (Puebla et al. 2007, 2011). However, the extent and nature of the X-ray flows are not fully justified in accordance with these new models. It has been suggested that the accretion flows in nonmagnetic white dwarf binaries are well explained in the context of radiatively inefficient advective hot flows in the X-ray regime (Balman & Revnivtsev 2012; Balman 2020; Mereghetti et al. 2021). This work is an extrapolation and development of our previous works on the two NLs regarding advection-dominated accretion flows in the X-rays (Balman et al. 2014; Godon et al. 2017). Such radiatively inefficient hot

<sup>6</sup> Corresponding author.



flow structure explains most of the complexities in the X-rays and other wavelengths as opposed to a standard optically thick accretion flow that is thought to exist in the inner disk of accreting white dwarf binaries (AWBs; see Balman 2020, for a review).

The nonmagnetic nova-likes (NLs) are found mostly in a state of high mass accretion rate (a few  $\times 10^{-8} M_{\odot} \text{ yr}^{-1}$  to a few  $\times 10^{-9} M_{\odot} \text{ yr}^{-1}$ ). The VY Scl-type subclass exhibits high states and occasional low states of optical brightness while the UX UMa subtype remains in the high state (Warner 1995). One of the two NLs discussed in this paper, BZ Cam is a VY Scl-type system whereas the other NL, V592 Cas, is of UX UMa type. All NLs show emission lines in the optical and/or UV wavelengths and signatures of winds in these bands. Bipolar outflows and/or rotationally dominated winds from NLs are detected typically in the FUV by the P Cygni profiles of the resonance doublet of CIV (Sion 1985). The mass-loss rates of the winds are  $\leq 1\%$  of the accretion rate, with velocities of 200–5000  $\text{ km s}^{-1}$  (Long & Knigge 2002; Kafka & Honeycutt 2004).

### 1.1. BZ Cam and V592 Cas

BZ Cam is an interesting NL classified as an VY Scl system among CVs with a period of 221 min (Patterson et al. 1996). It has a bow-shock nebula (Krautter et al. 1987; Griffith et al. 1995; Greiner et al. 2001), which is not consistent with a planetary nebula origin. New findings indicate that it may be associated with recurrent nova explosions of BZ Cam in timescales of millennia (Hoffmann & Vogt 2020; Tappert et al. 2020). Winds from BZ Cam are detected in the FUV resonance lines (as P Cygni profiles) along with the Balmer and He I lines. They show a bipolar nature with unsteady and continuously variable outflow of  $\sim 3000\text{--}5300 \text{ km s}^{-1}$  and show time variability from 100 s to 3000 s in the optical and UV indicating episodic behavior (Honeycutt et al. 2013). Greiner et al. (2001) present analysis of an optical low state, which shows that P Cygni profiles are absent in this state. Godon et al. (2017) find a WD temperature of 30000–45000 K using Far-Ultraviolet Spectroscopic Explorer (FUSE) and IUE data. The binary system has an inclination of about  $i = 12^{\circ}\text{--}40^{\circ}$ . A distance of  $830 \pm 160 \text{ pc}$  (Ringwald & Naylor 1998) was long accepted, but the GAIA archive<sup>7</sup> yields a distance of  $374 \pm 3 \text{ pc}$  using the parallax measurement (we will use the GAIA value in this paper).

V592 Cas is an UX UMa subtype with an inclination of  $i = 28^{\circ} \pm 10^{\circ}$  (Huber et al. 1998) and a period of 165 min (Taylor et al. 1998) with positive and negative superhumps. The GAIA distance is  $466 \pm 4 \text{ pc}$ . The mass of the WD in V592 Cas is about  $0.75 M_{\odot}$  with a temperature of 45,000 K (Hoard et al. 2009) and a mass accretion rate around  $1 \times 10^{-8} M_{\odot} \text{ yr}^{-1}$  (Taylor et al. 1998; Hoard et al. 2009). V592 Cas has a bipolar wind outflow, which is episodic and reaches velocities of  $5000 \text{ km s}^{-1}$  measured in H $\alpha$ . Moreover, the optical brightness variations and the strength of the outflow are not correlated (Kafka et al. 2009). V592 Cas was observed with IUE (Taylor et al. 1998) and FUSE (Prinja et al. 2004) revealing blueshifted absorption troughs in the UV with a nonsinusoidal behavior over the orbital phase. The outflowing wind does not show modulation over the negative or positive superhump periods of the source but is modulated on the orbital

period. Nevertheless, the system indicates the existence of a warped, precessing accretion disk.

### 1.2. Previous X-Ray Observations

At low mass accretion rates, nonmagnetic CV observations (i.e., dwarf nova in quiescence) have yielded hard X-ray spectra that show consistency with an optically thin multitemperature isobaric cooling flow model of plasma emission ( $kT_{\text{max}} \simeq 10\text{--}50 \text{ keV}$ ; see Pandel et al. 2005; Kuulkers et al. 2006; Balman et al. 2011; Wada et al. 2017; Balman 2020, and references therein). At high mass accretion rates ( $\dot{M}_{\text{acc}} \geq 10^{-9} M_{\odot} \text{ yr}^{-1}$ ), as opposed to expectations from standard steady-state accretion flow scenarios, observations of NLs have always shown a hot optically thin X-ray source (Patterson & Raymond 1985; van Teeseling et al. 1996). Furthermore, studies with data from ASCA, XMM-Newton, Chandra, and Swift have been modeled with double MEKAL models or multitemperature plasma models with luminosities  $\leq$  a few  $\times 10^{32} \text{ erg s}^{-1}$  (Mauche & Mukai 2002; Pratt et al. 2004; Page et al. 2014; Zemko et al. 2014; Balman et al. 2014; Dobrotka et al. 2017). In the light of these analyses of NLs, the optically thin hard X-ray emission with virial temperatures in the X-ray emitting region has been interpreted as the existence of ADAF-like radiatively inefficient advective accretion flows (RIAF ADAF) in the X-ray emitting zones near the WD (Balman et al. 2014; Balman 2015, 2020; Kimura et al. 2021). The existence of such RIAF ADAF-like flows and the transition radii into such nonstandard flows in CVs have also been articulated and studied using broadband noise analysis in nonmagnetic CV systems (mainly dwarf novae) by Balman & Revnivtsev (2012) and Balman (2015, 2020). This aperiodic timing variability is studied and reviewed in Balman (2019, 2020) where the break frequencies in the characteristic red noise structure of the power spectra show the change and the diminishing Keplerian flow in a standard Keplerian disk into a sub-Keplerian RIAF ADAF-like flow. The range of break frequencies are 1–6 mHz for quiescent dwarf novae translating to a transition radius of  $(3\text{--}10) \times 10^9 \text{ cm}$ .

The Swift XRT (X-ray) spectra of BZ Cam and V592 Cas have been found consistent with a multitemperature plasma emission model in collisional equilibrium at  $kT_{\text{max}} = 20\text{--}50 \text{ keV}$  within a 90% confidence level range, indicating that the X-ray emitting plasma is virialized (Balman et al. 2014). Swift does not detect any iron emission lines in the 6.0–7.0 keV range. In this study, a 7 eV upper limit for any blackbody temperature of a soft X-ray component was also calculated using ROSAT data of the two sources. The study also shows that the ratio  $L_x/L_{\text{disk}}$  ( $L_{\text{disk}}$  from the UV–optical wavelengths) yields considerable inefficiency of emission in the X-ray emitting region with  $\sim 0.01\text{--}0.001$ . This means that the accretion energy is stored in the flow. Balman et al. (2014) and Balman (2020) discuss that this energy goes into heating the WDs in the NLs or is directed to produce outflows or directed back to the outer disk aiding the production of the fast winds in these systems (see the discussion section of Balman et al. 2014 for details). The WDs in CVs cannot be heated more than 15% via accretional heating, and this value is limited to 1% for the very hot WDs as in these NLs (Godon & Sion 2003). If one scales the WD temperatures in our NLs (similar to most NLs) and the WD temperatures in polar-type magnetic CVs, which do not exhibit disk accretion in the 3–4 hr orbital period range, one finds that the ratio of the luminosities of the WDs is about 100 yielding a requirement for

<sup>7</sup> <https://gea.esac.esa.int/archive>

an inefficiency of 0.01 (Balman et al. 2014) in the X-ray emission to produce the excessive heating of WDs.

The power-law index of the temperature distribution shows departures from the isobaric cooling flow plasma in equilibrium as derived from the fits (Balman et al. 2014). In addition, a second component in the Swift X-ray spectra of BZ Cam recovered at about  $3\sigma$  significance is found consistent with a power-law emission, whereas V592 Cas has shown this second power-law component around  $2\sigma$ . As a result, the X-ray emitting regions in BZ Cam and V592 Cas (and in other NL systems) are interpreted as extended optically thin hard X-ray emitting regions of radiatively inefficient (ADAF-like) hot accretion flows and/or constitute X-ray corona regions in the inner disk in a fashion similar to X-ray binaries (Balman et al. 2014). Moreover, radiatively inefficient (ADAF-like) accretion flows can aid fast collimated outflows from disks as they have a positive Bernoulli parameter (the sum of the kinetic energy, potential energy and enthalpy), which can consistently explain the formation of  $3000\text{--}5300\text{ km s}^{-1}$  winds in BZ Cam and V592 Cas (and perhaps other NLs) that are also variable and episodic in nature.

## 2. The Observation and Data

BZ Cam and V592 Cas were observed with NuSTAR on 2017 April 29 and 2016 August 28, respectively. NuSTAR is the first focusing hard X-ray space observatory launched on 2012 June 13 (Harrison et al. 2013) and hosts two co-aligned optical crystal detectors focused onto two focal planes, Focal Plane Module A (FPMA) and B (FPMB). It covers the energy range 3–79 keV with an effective area summed over the two modules of about  $900\text{ cm}^2$  around 10 keV. It has an energy resolution of 400 eV at 10 keV and 900 eV at 68 keV with an angular resolution of  $18''$  (FWHM). For BZ Cam, the source exposure times were 37.8 ks and 37.7 ks for FPMA and FPMB, respectively (ID=30201010002, PI=Balman). The FPMA and FPMB exposures were 39.5 and 39.4 for V592 Cas (ID=30201012002, PI=Balman). The data were processed using NuSTARDAS version 1.7.1, 1.8.0, and CALDB 20170727. The *nupipeline* tool was run to generate cleaned event lists and remove passages from the South Atlantic Anomaly. The *nuproducts* tool was used to extract background and source spectra and light curves together with the appropriate response (RMF) and ancillary (ARF) files. To extract photons for the source and background devoid of contaminations, circular regions with radii  $73''\text{--}135''$  for BZ Cam and  $50''\text{--}100''$  for V592 Cas were used. The background counts were extracted from different parts of the detector, and the extraction sizes were studied and optimized for a proper source and background extraction (as to maximize the count rate and statistical quality). We assumed the largest extraction radii in these ranges for the fitted spectra. There were no stray light contaminations associated with the observations. Further data reductions were performed using HEASoft<sup>8</sup> (version 6.20-6.24). In order to increase the S/N in the spectrum, the FPMA/B spectra were combined using HEASoft task *addspec*, which produced proper response and ancillary files. This step was inspected carefully as to how well the FPMA/B spectra were incorporated together using the original spectral files of FPMA/B and comparative analysis (using proper response and

ancillary files). The net source count rates were  $0.113(2)\text{ c s}^{-1}$  and  $0.071(2)\text{ c s}^{-1}$  for BZ Cam and V592 Cas, respectively.

As second and third observations, we used Swift XRT and ROSAT data of BZ Cam and V592 Cas that were published in Balman et al. (2014) in detail, to cover the soft energy ranges and calibrate the spectral fits better. Swift XRT is a focusing X-ray telescope with a  $110\text{ cm}^2$  effective area at 1.5 keV and a  $24'$  field of view in the 0.3–10.0 keV energy range (Burrows et al. 2005). The data were obtained in the PC (photon counting mode) with full imaging capacity. The source exposures were 15 ks, and the net count rates were  $0.069(3)\text{ c s}^{-1}$  and  $0.051(2)\text{ c s}^{-1}$ , for BZ Cam and V592 Cas, respectively. The ROSAT count rates were similar with  $0.078(4)\text{ c s}^{-1}$  (BZ Cam) and  $0.048(8)\text{ c s}^{-1}$  (V592 Cas) in the 0.1–2.0 keV band. BZ Cam observation (ID=rp300233n00) was performed on 1992 September 28–29 (not a low state) using the PSPCB detector (6.0 ks). Data of V592 Cas (ID=rs930701n00) were obtained during the RASS (ROSAT all sky survey; 1990 December 29 to 1991 August 06) using the PSPCC detector (0.6 ks). The spectra for Swift and ROSAT were extracted and analyzed using similar versions of HEASoft and XSELECT<sup>9</sup> v2.4-e.

## 3. Spectral Analysis

As described in the previous section, source and background spectra, response, and ancillary files were generated for BZ Cam and V592 Cas using the *nuproducts* tool for the NuSTAR data. Subsequently, the FPMA/B spectra were combined. The combined spectra were grouped to yield an S/N ratio of 10–12 in each spectral bin to acquire good  $\chi^2$  statistics. The soft energies not covered by NuSTAR were supplemented with the ROSAT PSPC and Swift XRT data published and/or used in Balman et al. (2014). The spectral extraction of the Swift XRT spectra are summarized in Section 6 of this paper. Spectra grouped to have a minimum of 30 counts in each bin are used in this paper, whereas the fits in Balman et al. (2014) were performed on spectra with 60 counts in each bin. This is done to utilize the spectral resolution of the data for a better match to NuSTAR data. ROSAT data are used to accommodate for the softest X-ray energies in conjunction with the other two observatory data. A grouping of 10–20 counts in each bin is used to achieve adequate statistics. The spectral analysis of the joint spectra are done within the XSPEC software (for references and model descriptions see Arnaud 1996<sup>10</sup>). To account for the interstellar absorption in the broadband X-ray spectra, the *tbabs* model was utilized in the fitting procedures (abundances set to “wilm”; Wilms et al. 2000). During the entire spectral analysis, constant multiplicative model factors have been incorporated in the fits to account for the cross-normalization calibration between different observatory data. We caution that we do not expect a change in the long-time variability characteristics of our sources (i.e., high or low states) as mentioned in the introduction and Section 1.1. Moreover, we do not find any sporadic events or flare-type events in any of the observations included from the three missions used in this study.

As the first step, joint X-ray spectra (ROSAT+Swift+NuSTAR) of BZ Cam and V592 Cas are modeled with the multitemperature isobaric cooling flow type of plasma emission model CEVMKL in XSPEC (Liedahl et al. 1995; Singh et al. 1996) as was done for the Swift analysis (i.e., *tbabs* × CEVMKL; Balman et al. 2014). We

<sup>8</sup> <https://heasarc.gsfc.nasa.gov/docs/software/heasoft/>

<sup>9</sup> <https://heasarc.gsfc.nasa.gov/ftools/xselect/>

<sup>10</sup> <https://heasarc.gsfc.nasa.gov/xanadu/xspec/manual/Models.html>

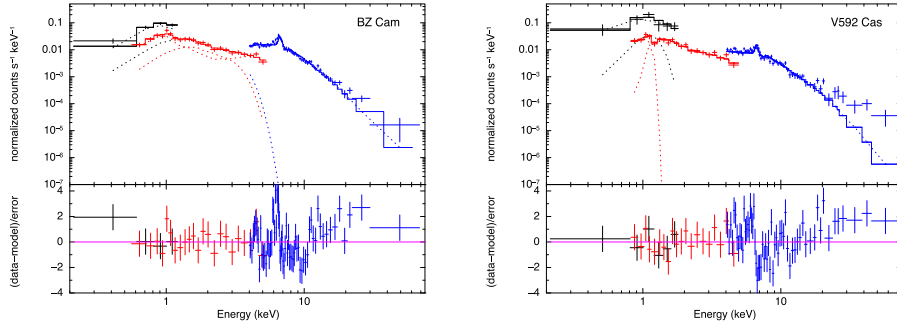


**Figure 1.** The left-hand panel is the fitted ROSAT, Swift, and NuSTAR (combined) spectra of BZ Cam using the *tbabs*  $\times$  CEVMKL model. The right-hand panel is the fitted V592 Cas spectra. The dotted lines show the individual model components, the crosses are the data (black for ROSAT, red for Swift, and blue for NuSTAR), and the solid lines indicate the fitted spectrum. The lower panels show the residuals in standard deviations.

assumed “switch set to 2” where the CEVMKL model uses the APEC model for interpolation with the ATOMDB<sup>11</sup> database. The fits with the CEVMKL model are conducted between 0.2 and 75.0 keV yielding unacceptable values above  $\chi^2_{\nu} \sim 2.0$  with large sigma deviations around the iron line complex between 6.0–7.0 keV for both sources. The spectral parameters of the fit are  $kT_{\max} = 28\text{--}38$  keV and  $\alpha < 0.02$  for V592 Cas at a 90% confidence level ( $\alpha$  is the power-law index parameter for the temperature distribution, which is expected to be 1.0 for a cooling flow type of plasma). For BZ Cam, these parameters are  $kT_{\max} = 14\text{--}19$  keV and  $\alpha < 0.04$  at the same confidence level. In the fitting procedure, we assumed fixed solar abundances as the fits were not sensitive to changing abundances (e.g., iron) where the error ranges include solar abundances.

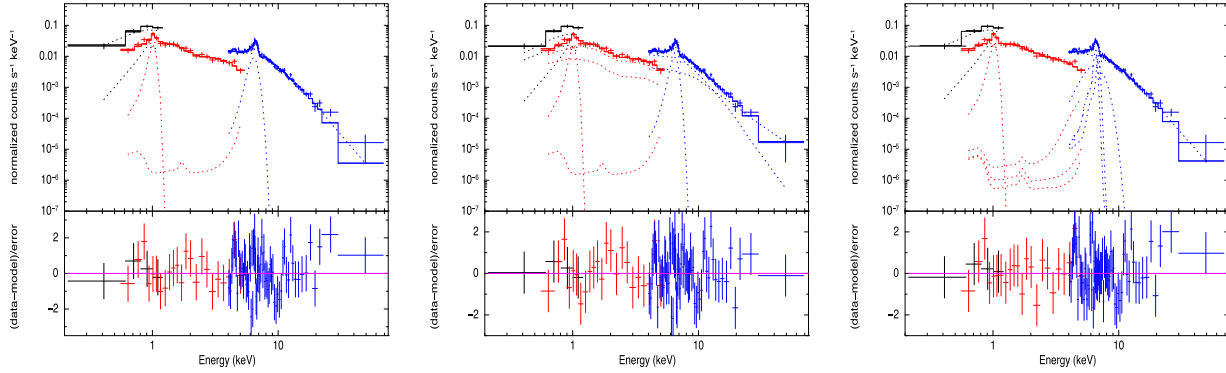
The low  $\alpha$  values are nonphysical for CEVMKL model indicating significant lack of radiative cooling in the plasma meaning changes in differential emission measures ( $\propto L$ ) are very small with changing temperature. The continuous temperature distribution in the X-rays described with the CEVMKL model is an isobaric cooling flow-type plasma model in collisional equilibrium with a differential emission measure that depends on a power-law distribution of temperatures ( $dEM = (T/T_{\max})^{\alpha-1} dT/T_{\max}$ ). In such a model, the emission measure at each temperature is proportional to the time the cooling gas remains at this temperature (Pandel et al. 2005). The fitted spectra are displayed in Figure 1. Our analysis shows that the *tbabs*  $\times$  CEVMKL model fits are inadequate. Moreover, such large deviations in the residuals around the 6.0–7.0 keV complex are indicative of nonequilibrium ionization conditions in the plasma flow, as CEVMKL is a collisional ionization equilibrium plasma emission (CIE) model. Consequently, the CEVMKL model is not used for further analysis as it does not fit the continuum and the iron line complex successfully. Next, we inspected the behavior of residuals around the iron line complex indicative of other emission and absorption features and added one Gaussian absorption line, using the GABS model, and two to three emission lines, using the GAUSS model, to account for the variations in the residuals. Along these line models, we assumed a Bremsstrahlung continuum model (free–free emission), BREMSS (in XSPEC), and a nonequilibrium ionization plasma emission model, VNEI (in XSPEC). The Swift spectra are also fitted better with the addition of neon or iron emission and

absorption line features represented with other GABS and GAUSS models in the fitting procedure. The composite model fits to the joint ROSAT, Swift, and NuSTAR spectra are displayed in Figures 2 and 3, and the results of the spectral fits are given in Tables 1 and 2, for BZ Cam and V592 Cas, respectively.

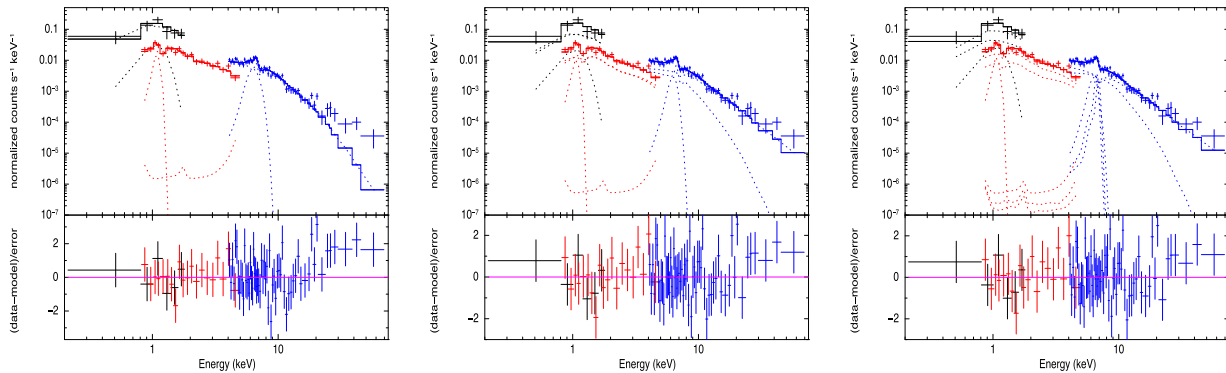
### 3.1. BZ Cam

Table 1 shows two composite model fits performed on the joint ROSAT, Swift, and NuSTAR spectra of BZ Cam that describe the conditions in the X-ray emitting region. We used Fit-1 that includes a nonequilibrium ionization (NEI) plasma model (VNEI in XSPEC) as the CEVMKL (CIE model) model fails to fit the composite spectra. Deviations from standard CIE plasma line profiles are expected in NEI hot flows. Thus, we included emission line and absorption line components to the composite models until the residual fluctuations ( $2\sigma\text{--}3\sigma$ ) around the lines were reduced. As Fit-1 represents a more physical model for the plasma flow in the X-ray emitting region where only an absorption line of Fe, the iron reflection line at 6.4 keV and an absorption feature at around 1.14–1.25 were included for a satisfactory fit. Fit-2 is utilized to model all the detected emission and absorption features with a free–free continuum model that is Bremsstrahlung (BREMSS in XSPEC). We note that a power-law model for the continuum can also be assumed for the same fit but it does not change the modeled line structure in Fit-2 and does not significantly improve the fit. The spectral analysis reveals that a lower plasma temperature in a range 8.2–9.4 keV is obtained with the VNEI model instead of 14–19 keV derived from the CEVMKL model fit. The NEI model fits yield lower plasma temperatures in comparison with CIE model fits as a result of the plasma ionization conditions (i.e., underionized). We note that we have used solar abundances all throughout the fitting procedures for both NL sources as the fits are not sensitive to abundance variations where error ranges include solar values. Overall, Fit-1 improves at a  $3\sigma$  significance when a power-law model is added to the fit ( $F$ – $T$  test yields improvement at a 99.3% confidence level). This indicates the existence of Compton up/downscattering in the system. However, Fit-2 is better than Fit-1 at 97.9% confidence level; thus an additional power-law model exists only if NEI plasma is assumed and a fully ionized plasma (as in BREMSS model description) is adequate to

<sup>11</sup> <http://atomdb.org>



**Figure 2.** The left-hand panel is the fitted ROSAT, Swift, and NuSTAR (joint) spectra of BZ Cam using the model  $tbabs \times GABS \times GABS(VNEI+GAUSS)$ . The middle panel is the joint spectra fitted with the composite model  $tbabs \times GABS \times GABS(VNEI+power+GAUSS)$ , and the right-hand panel shows the same spectra fitted with the model  $tbabs \times GABS \times GABS(BREMS+GAUS+GAUS+GAUS+GAUS)$  as listed in Table 1. The dotted lines show the individual model components, the crosses are the data (black for ROSAT, red for Swift, and blue for NuSTAR), and the solid lines indicate the fitted spectrum. The lower panels show the residuals in standard deviations.



**Figure 3.** The left-hand panel is the fitted ROSAT, Swift, and NuSTAR (joint) spectra of V592 Cas using the model  $tbabs \times GABS \times GABS(VNEI+GAUSS)$ . The middle panel is the joint spectra fitted with the composite model  $tbabs \times GABS \times GABS(VNEI+power+GAUSS)$ , and the right-hand panel shows the same spectra fitted with the model  $tbabs \times GABS \times GABS(BREMS+power+GAUS+GAUS+GAUS+GAUS)$  as listed in Table 2. The dotted lines show the individual model components, the crosses are the data (black for ROSAT, red for Swift, and blue for NuSTAR), and the solid lines indicate the fitted spectrum. The lower panels show the residuals in standard deviations.

explain the continuum emission (however, not the line emission).

In addition, we detect the iron  $K\alpha$  reflection line at around 6.3–6.5 keV in Fit-1 and Fit-2. The Gaussian line widths,  $\sigma$ , are different as calculated by the two fits, where Fit-1 yields 0.2–0.4 keV and Fit-2  $0.8 < \sigma < 1.0$  keV, respectively. The large width in Fit-2 is indicative of scattering in an accretion disk corona, but the smaller widths in both of Fit-1, portray broadening in the inner regions of the accretion disk as the flow is extended and has higher viscosity or it is scattering off the existing wind outflow. The Gaussian line sigma for the reflection line from Fit-2 and Fit-1 are both inconsistent with Doppler broadening, which yields disk radii inside the WD (i.e., too fast a rotation). The mass of the WD (0.4–0.7  $M_{\odot}$ ) and the locations where the lines are produced are unlikely for any gravitational redshift interpretation. Thus, the iron  $K\alpha$  line widths are indicative of scattering in the system within the advective hot flow that is extended or the reflection off the cooler parts of the disk, or scattering from the wind outflow itself. Reflection off of the

accretion disks in active galactic nuclei (AGNs) and X-ray binaries (XRBs) are well studied and reveal a Compton reflection spectrum over 0.1–10 keV with a hump around 20–30 keV, which is a strong function of the photon index of the incident spectrum, iron abundance, line-of-sight angle, and ionization level in the reflected spectrum (see Ross & Fabian 2005; Kinch et al. 2016). A reflection broadband spectrum can be justified for BZ Cam owing to the iron reflection line and the additional power-law emission (or the large line width with the free-free continuum); however the Compton hump around 20–30 keV is not significant. Fits using simple reflection models within XSPEC (e.g., *reflect*) do not produce any better fits than those in Table 1, and some reflection models are not suitable for AWBs.

### 3.2. V592 Cas

Following the spectral analysis of BZ Cam, the analysis of V592 Cas has been conducted in the same manner with the same models (see Table 2) except that this time there is a need

**Table 1**  
Spectral Parameters of the Fits to the Joint ROSAT, NuSTAR, and Swift Spectra of BZ Cam

Model	Parameter	Fit-1 <sup>a</sup>	Fit-1 <sup>b</sup>	Fit-2 <sup>c</sup>
TBabs	$N_H$ ( $10^{22} \text{ cm}^{-2}$ )	$0.06^{+0.03}_{-0.01}$	$0.09^{+0.03}_{-0.03}$	$0.08^{+0.03}_{-0.02}$
VNEI	kT (keV)	$8.8^{+0.6}_{-0.6}$	$5.9^{+0.6}_{-0.5}$	N/A
	$\tau$ ( $s \text{ cm}^{-3}$ )	$3.9^{+2.0}_{-1.0} \times 10^{11}$	$3.8^{+5.2}_{-1.2} \times 10^{11}$	N/A
	$K_{\text{VNEI}}$	$2.1^{+0.1}_{-0.2} \times 10^{-3}$	$2.0^{+0.3}_{-0.2} \times 10^{-3}$	N/A
BREMSS	kT (keV)	N/A		$9.7^{+0.7}_{-0.6}$
	$K_{\text{BREMSS}}$	N/A	N/A	$6.3^{+0.4}_{-0.3} \times 10^{-4}$
Power Law	Photon Index	N/A	$1.81^{+0.06}_{-0.05}$	N/A
	$K_{\text{powerlaw}}$	N/A	$2.4^{+0.4}_{-0.4} \times 10^{-4}$	N/A
GABS	LineE (keV)	1.15 (fixed)	1.15 (fixed)	$1.22^{+0.16}_{-0.17}$
	$\sigma$ (keV)	$1.20^{+0.2}_{-0.2}$	$1.5^{+0.2}_{-0.1}$	0.5 (fixed)
	depth	$1.6^{+0.3}_{-0.3}$	$3.3^{+0.5}_{-0.4}$	$0.5^{+0.2}_{-0.1}$
GABS	LineE (keV)	$7.05^{+0.10}_{-0.05}$	$7.05^{+0.08}_{-0.08}$	$7.02^{+0.01}_{-0.01}$
	$\sigma$ (keV)	$0.001^{+0.013}_{>}$	$0.001^{+0.013}_{>}$	$0.06^{+0.04}_{-0.03}$
	depth	$1.0^{+2.0}_{>}$	$0.04^{+1.1}_{>}$	$1.0^{+0.15}_{-0.13}$
GAUSS	LineE (keV)	$1.01^{+0.02}_{-0.03}$	$1.01^{+0.02}_{-0.03}$	$1.01^{+0.02}_{-0.02}$
	$\sigma$ (keV)	$0.001^{+0.06}_{>}$	$0.001^{+0.05}_{>}$	$0.001^{+0.07}_{>}$
	$K_{\text{Gauss}}$	$6.7^{+2.3}_{-2.4} \times 10^{-5}$	$9.0^{+4.0}_{-3.0} \times 10^{-5}$	$6.6^{+2.0}_{-2.0} \times 10^{-5}$
GAUSS	LineE (keV)	$6.38^{+0.06}_{-0.08}$	$6.46^{+0.05}_{-0.07}$	$6.38^{<}_{-0.2}$
	$\sigma$ (keV)	$0.3^{+0.07}_{-0.07}$	$0.3^{+0.1}_{-0.1}$	$1.0^{<}_{-0.2}$
	$K_{\text{Gauss}}$	$1.9^{+0.4}_{-0.3} \times 10^{-5}$	$2.2^{+0.4}_{-0.3} \times 10^{-5}$	$2.9^{+0.8}_{-0.7} \times 10^{-5}$
GAUSS	LineE (keV)	N/A	N/A	$6.89^{+0.02}_{-0.01}$
	$\sigma$ (keV)	N/A	N/A	$0.01^{+0.05}_{>}$
	$K_{\text{Gauss}}$	N/A	N/A	$2.6^{+0.5}_{-0.4} \times 10^{-5}$
GAUSS	LineE (keV)	N/A	N/A	$6.55^{+0.02}_{-0.03}$
	$\sigma$ (keV)	N/A	N/A	$0.01^{+0.09}_{>}$
	$K_{\text{Gauss}}$	N/A	N/A	$1.6^{+0.3}_{-0.2} \times 10^{-5}$
	$\chi^2_\nu(\nu)$	1.37 (93)	1.28 (92)	1.20 (90)
Flux (thermal)	( $10^{-12}$ ) $\text{erg cm}^{-2} \text{s}^{-1}$	$5.5^{+0.5}_{-0.7}$	$4.7^{+0.7}_{-0.3}$	$5.1^{+1.1}_{-0.6}$
Luminosity	(ther.)	( $10^{32} \text{ erg s}^{-1}$ )	0.74-1.02	
Flux (nonther.)	( $10^{-12}$ ) $\text{erg cm}^{-2} \text{s}^{-1}$	N/A	$2.9^{+0.3}_{-0.2}$	N/A
Luminosity	(nonther.)	( $10^{32} \text{ erg s}^{-1}$ )	0.46-0.54	

**Notes.** *tbabs*–(abund = wilms) (Wilms et al. 2000). Solar abundances are assumed in the plasma models when necessary. Fits are performed using ROSAT, Swift, and NuSTAR data in the 0.2–75.0 keV range. The *NEIvers.3.0.9* plasma code with the ATOMDB database was assumed for VNEI fits.  $N_H$  is the absorbing column,  $\tau$  is the ionization timescale ( $n_e t$ ),  $K_{\text{Gauss}}$ ,  $K_{\text{VNEI}}$ , and  $K_{\text{BREMSS}}$  are the normalizations for the Gaussian line, VNEI, and BREMSS models. The normalization constants of the VNEI and BREMSS models are in  $K = (10^{-14}/4\pi D^2) \times \text{EM}$ , where EM (emission measure) =  $\int n_e n_H dV$  (integration is over the emitting volume  $V$ ). All errors are calculated at 90% confidence level for a single parameter. The unabsorbed X-ray flux and the luminosities are given in the range 0.1–100.0 keV. For luminosities, the distance of 374 pc is assumed (see Section 1).

<sup>a</sup> *tbabs* × GABS × GABS(VNEI+GAUSS).

<sup>b</sup> *tbabs* × GABS × GABS(VNEI+power+GAUSS).

<sup>c</sup> *tbabs* × GABS × GABS(BREMSS+GAUSS+GAUSS+GAUSS+GAUSS).

for an additional power-law model along with the BREMSS model assumed for the continuum as referenced in the Table 2 comments. We also note that including the H-like iron line in the Fit-2 has low significance (at only  $1\sigma$ ); thus there is only a significant He-like iron line, which can be derived from the fits. The width of the H-like and He-like iron (for both of Fit-2) has been kept fixed at around their best-fit parameters as is revealed by the narrow line structure limited with the spectral resolution of NuSTAR at these energies. Fit-1, which is the VNEI model fit, yields a plasma temperature in a range 11.1–12.9 keV with an

ionization timescale of  $(1.7\text{--}3.2) \times 10^{11} \text{ cm s}^{-3}$ . This timescale is indicative of nonequilibrium conditions. The ionization timescale of BZ Cam is also  $(2.9\text{--}5.9) \times 10^{11} \text{ cm s}^{-3}$  and shows existence of a plasma flow that has not reached ionization equilibrium. An additional power-law model included in Fit-1 for V592 Cas is significant at a 98.9% confidence level and in Fit-2 at a 99% confidence level, which reveals a power-law component at high significance. Such an additional component exists significantly for BZ Cam if the VNEI model is assumed. The range of photon indices are 1.5–1.8 for V592 Cas and 1.76–1.87 for BZ Cam.

**Table 2**  
Spectral Parameters of the Fits to the Joint ROSAT, NuSTAR, and Swift Spectra of V592 Cas

Model	Parameter	Fit-1 <sup>a</sup>	Fit-1 <sup>b</sup>	Fit-2 <sup>c</sup>	Fit-2 <sup>d</sup>
TBabs	$N_H$ ( $10^{22} \text{ cm}^{-2}$ )	$0.16^{+0.09}_{-0.07}$	$0.40^{+0.06}_{-0.13}$	$0.21^{+0.08}_{-0.08}$	$0.31^{+0.10}_{-0.09}$
VNEI	kT (keV)	$11.4^{+1.5}_{-1.3}$	$4.9^{+1.2}_{-1.4}$	N/A	N/A
	$\tau$ (s $\text{cm}^{-3}$ )	$2.2^{+1.0}_{-0.5} \times 10^{11}$	$3.8^{<1.2}_{-1.2} \times 10^{11}$	N/A	N/A
	$K_{\text{VNEI}}$	$1.3^{+0.1}_{-0.1} \times 10^{-3}$	$6.2^{+2.7}_{-1.0} \times 10^{-3}$	N/A	N/A
BREMSS	kT (keV)	N/A	N/A	$10.9^{+1.4}_{-1.1}$	$5.0^{+1.1}_{-1.0}$
	$K_{\text{BREMSS}}$	N/A	N/A	$5.0^{+0.3}_{-0.4} \times 10^{-4}$	$3.7^{+0.4}_{-0.4} \times 10^{-4}$
Power Law	Photon Index	N/A	$1.74^{+0.06}_{-0.06}$	N/A	$1.56^{+0.05}_{-0.06}$
	$K_{\text{powerlaw}}$	N/A	$2.3^{+0.3}_{-0.3} \times 10^{-4}$	N/A	$1.4^{+0.2}_{-0.3} \times 10^{-4}$
GABS	LineE (keV)	$1.16^{+0.03}_{-0.02}$	$1.2^{+0.05}_{-0.05}$	$1.18^{+0.07}_{-0.04}$	$1.22^{+0.04}_{-0.06}$
	$\sigma$ (keV)	0.01 (fixed)	0.01 (fixed)	0.01 (fixed)	0.01 (fixed)
	depth	$6721.7^{<6714.7}$	$107.6^{<107.2}$	$39.6^{<26.4}$	$14.2^{<14.1}$
GABS	LineE (keV)	$6.9^{+0.1}_{-0.1}$	$7.09^{+0.25}_{-0.25}$	$6.98^{+0.05}_{-0.05}$	$7.00^{+0.04}_{-0.06}$
	$\sigma$ (keV)	$0.7^{+0.1}_{-0.1}$	$0.2^{+0.06}_{-0.1}$	$0.16^{+0.06}_{-0.08}$	$0.12^{+0.1}_{-0.05}$
	depth	$1.3^{+0.2}_{-0.2}$	$2.80^{<2.78}$	$0.4^{+0.2}_{-0.1}$	$0.34^{+0.11}_{-0.09}$
GAUSS	LineE (keV)	$1.08^{+0.02}_{-0.04}$	$1.06^{+0.05}_{-0.06}$	$1.07^{+0.04}_{-0.03}$	$1.06^{+0.05}_{-0.04}$
	$\sigma$ (keV)	0.01 (fixed)	0.01 (fixed)	0.01 (fixed)	0.01 (fixed)
	$K_{\text{Gauss}}$	$2.8^{+1.4}_{-1.4} \times 10^{-5}$	$2.8^{+1.6}_{-2.3} \times 10^{-5}$	$3.0^{+1.5}_{-1.5} \times 10^{-5}$	$2.8^{+1.9}_{-1.8} \times 10^{-5}$
GAUSS	LineE (keV)	$6.5^{+0.1}_{-0.10}$	$6.38^{+0.09}_{-0.23}$	$6.4^{+0.2}_{-0.2}$	$6.36^{+0.18}_{-0.19}$
	$\sigma$ (keV)	$0.5^{+0.1}_{-0.1}$	$0.4^{+0.2}_{-0.2}$	$0.4^{+0.2}_{-0.1}$	$0.4^{+0.2}_{-0.2}$
	$K_{\text{Gauss}}$	$3.4^{+0.6}_{-0.6} \times 10^{-5}$	$8.0^{+1.2}_{-3.5} \times 10^{-5}$	$9.7^{+3.6}_{-3.4} \times 10^{-6}$	$7.2^{+2.6}_{-2.5} \times 10^{-6}$
GAUSS	LineE (keV)	N/A	N/A	$6.88^{+0.11}_{-0.04}$	$6.89^{+0.08}_{-0.05}$
	$\sigma$ (keV)	N/A	N/A	0.001 (fixed)	0.001 (fixed)
	$K_{\text{Gauss}}$	N/A	N/A	$9.1^{+4.1}_{-3.8} \times 10^{-6}$	$5.9^{+2.9}_{-2.6} \times 10^{-6}$
GAUSS	LineE (keV)	N/A	N/A	$6.64^{+0.02}_{-0.08}$	$6.63^{+0.08}_{-0.07}$
	$\sigma$ (keV)	N/A	N/A	0.001 (fixed)	0.001 (fixed)
	$K_{\text{Gauss}}$	N/A	N/A	$5.4^{+2.2}_{-1.9} \times 10^{-6}$	$4.0^{+1.6}_{-1.4} \times 10^{-5}$
	$\chi^2_\nu(\nu)$	1.71 (109)	1.60 (107)	1.76 (106)	1.64 (104)
Flux (thermal)	( $10^{-12}$ ) erg $\text{cm}^{-2}\text{s}^{-1}$	$3.9^{+0.5}_{-0.2}$	$1.6^{+0.3}_{-0.3}$	$4.1^{+0.6}_{-0.6}$	$2.1^{+0.6}_{-0.3}$
Luminosity Flux (nonther.)	(ther.) ( $10^{-12}$ ) erg $\text{cm}^{-2}\text{s}^{-1}$	( $10^{32}$ erg $\text{s}^{-1}$ ) N/A	0.92-1.23 (no pow) $4.0^{+0.2}_{-0.1}$	0.34-0.71 (with pow) N/A	$3.6^{+0.3}_{-0.2}$
Luminosity	(nonther.)	( $10^{32}$ erg $\text{s}^{-1}$ )		0.89–1.1	

**Notes.** *tbabs*–(abund = wilm) (Wilms et al. 2000). Solar abundances are assumed in the plasma models when necessary. Fits are performed using ROSAT, Swift, and NuSTAR data in the 0.2–75.0 keV range. The NEIvers.3.0.9 plasma code with the ATOMDB database was assumed for VNEI fits.  $N_H$  is the absorbing column,  $\tau$  is the ionization timescale ( $n_e t$ ),  $K_{\text{Gauss}}$ ,  $K_{\text{VNEI}}$ , and  $K_{\text{BREMSS}}$  are the normalizations for the Gaussian line, VNEI, and BREMSS models. The normalization constants of the VNEI and BREMSS models are in  $K = (10^{-14}/4\pi D^2) \times \text{EM}$ , where EM (emission measure) =  $\int n_e n_H dV$  (integration is over the emitting volume  $V$ ). All errors are calculated at 90% confidence level for a single parameter. The unabsorbed X-ray flux and the luminosities are given in the range 0.1–100.0 keV. For luminosities, the distance of 466 pc is assumed (see Section 1).

<sup>a</sup> *tbabs* × GABS × GABS(VNEI+GAUSS).

<sup>b</sup> *tbabs* × GABS × GABS(VNEI+power+GAUSS).

<sup>c</sup> *tbabs* × GABS × GABS(BREMSS+GAUSS+GAUSS+GAUSS+GAUSS).

<sup>d</sup> *tbabs* × GABS × GABS(BREMSS+power+GAUSS+GAUSS+GAUSS+GAUSS).

Note that the fitted plasma temperatures become lower once the power-law component is included in the fits (see Tables 1 and 2). V592 Cas shows a 6.2–6.5 keV iron  $K\alpha$  line as in BZ Cam. The Gaussian line width,  $\sigma$ , is 0.2–0.4 keV revealing a similar origin of scattering in the system within the extended advective hot flow or reflection off the disk and reflection off the wind outflow. Similar with BZ Cam, the reflection line width shows no consistency with Doppler broadening or gravitational redshift effects. We note that using simple reflection models as in the analysis of BZ Cam does not improve the fits in Table 2.

Fit-1 and Fit-2 show the existence of a Gaussian absorption line ( $2\sigma$ – $3\sigma$  significance) with a centroid of 6.97–7.13 keV and 6.94–7.05 keV for BZ Cam and V592 Cas, respectively, in the vicinity of the H-like iron emission line that is at 6.97 keV (Fe XXVI). The absorption line widths ( $\sigma$ ) of 0.4–0.08 keV for V592 Cas and 0.1–0.03 keV for BZ Cam, indicate a wider line for V592 Cas and plausibly different conditions in the region of origin and a different geometry that is responsible for the absorption. Furthermore, the fits yield another absorption feature at around 1.1–1.25 keV in both sources, which may

correspond to Ne H $\beta$  line or other iron L-shell lines that fall in these energies. In addition, an emission line is detected in the fits for both of the sources around 0.98–1.03 keV for BZ Cam and 1.00–1.1 keV for V592 Cas, which is in accordance with Ne X (H-like Ne) emission line or some iron L-shell emission line.

Finally, we note that NuSTAR spectra of both of the NLs can be fitted alone with two main spectral components of a thermal plasma and a power law yielding power-law photon indices in the range 1.85–2.2. The significant power-law components from the Swift analysis are already mentioned in Section 1.2. The neutral hydrogen column density in the line of sight for BZ Cam and V592 Cas was thoroughly discussed in Balman et al. (2014) and will not be repeated here, but the values derived from the fits given on Tables 1 and 2 are consistent with absorption by the interstellar medium, and we do not find any intrinsic neutral hydrogen column density that could yield absorption of any alleged soft X-ray emission component.

#### 4. Aperiodic Variability in the Accretion Flow

Analysis of aperiodic variability and broadband noise have been used as a diagnosis technique for understanding disk structure and state transitions in accreting binaries. Long-timescale variability in CV disks may be created in the outer parts of the accretion disk, but the relatively short-time variability (at  $f > \text{few mHz}$ ), intrinsic to the disk, originates in the inner parts of the accretion disk (see Balman & Revnivtsev 2012; Scaringi et al. 2012; Dobrotka et al. 2012; Balman 2015; Bruch 2015; Baptista 2016; Dobrotka et al. 2016; Balman 2019, and references therein). Properties of this noise are similar to those of X-ray binaries with neutron stars and black holes. The model of origin for this aperiodic noise is the model of propagating fluctuations (Lyubarskii 1997; Revnivtsev et al. 2009, 2010; Uttley et al. 2011; Ingram & Done 2011; Ingram & van der Klis 2013; Ingram 2016). Variations in the mass accretion rate as a result of fluctuations are inserted into the flow at all Keplerian radii of the accretion disk due to the nature of its viscosity and then transferred toward the compact object. In this prescription, optically thick accretion flows are expected to show a frequency index of  $f^{-1 \dots -1.3}$  in the power spectral distribution of the red noise (Churazov et al. 2001; Gilfanov & Arefiev 2005; Gilfanov 2010). Once the optically thick flow subsides (truncates in a region/radius), the broadband noise as a result of aperiodic variability of the flow that has a power-law ( $\sim 1/f$ ) frequency distribution will show a break (red noise, which shows the characteristic of the optically thick flow variability, will show a break from the  $1/f$  dependence). It is expected that red noise will diminish as a result of lack of aperiodic variability from the optically thick flow. This red noise (power law) will show a break into a steeper (e.g.,  $1/f^2$  van der Klis 2006) power-law regime in higher frequencies. Unless another noise component takes over. Historically, truncation of the optically thick accretion disk in DNe in quiescence was introduced as an explanation for the time lags between the optical and UV fluxes in the rise phase of the outbursts (Meyer & Meyer-Hofmeister 1994; Stehle & King 1999), and for some implications of the disk instability model (DIM; Lasota 2004).

CVs demonstrate band-limited noise (noise structure that steeply decreases or shows a break toward high frequencies) in the optical, UV, and X-ray energy bands, which can be

adequately explained in the framework of the model of propagating fluctuations. Detailed modeling and results can be found in Scaringi et al. (2012), Balman & Revnivtsev (2012), Balman (2015), Semena et al. (2016), and Balman (2019). The detected frequency breaks in the nonmagnetic CVs (mainly DNe) are in the range (1–6) mHz in quiescence and indicate an optically thick disk truncation (i.e., transition) showing existence of the advective hot flows (RIAF ADAF-like flows) in the inner regions. Analysis of available data (e.g., SS Cyg, SU UMa, WZ Sge) reveal that during the outburst the inner (optically thick) disk radius moves toward the white dwarf and recedes as the outburst declines (Balman 2019) while linked changes in the X-ray energy spectra are also observed. Cross correlations between the simultaneous optical, UV, and X-ray light curves show time lags (propagation lags about 1.5–3 minutes) consistent with truncated optically thick disk and transition to advective hot flows in the inner disk (see Balman 2020, for a final review). The aperiodic variability characteristics of NLs have not been studied in detail (using the propagating fluctuations model) except for MV Lyr (Scaringi et al. 2012, 2013) in the optical revealing several quasiperiodic oscillation (QPO) structures and a break in the frequencies roughly around 1 mHz. Here, we study the power spectral characteristics using the NuSTAR data of both BZ Cam and V592 Cas and include the analysis of MV Lyr for comparisons.

In order to study the noise structure of the power spectra (PDS), we prepared source and background light curves with the *nuproducts* task using the standard procedures of NuSTAR analysis for each source, MV Lyr, BZ Cam, and V592 Cas as discussed in Section 2. The background-subtracted light curves were calculated using FTOOLS, and power spectral analysis was done utilizing the XRONOS<sup>12</sup> software package and the *powspec* task as part of HEASoft. During the timing analysis, the background-subtracted FPMA/B light curves were used simultaneously. The PDS were calculated in terms of the fractional rms amplitude squared per Hertz following the Miyamoto et al. (1991) normalization (see also Belloni & Hasinger 1990). While calculating the final PDS, the light curves were divided into segments using 1–2 s binnings in time and a total bin number per PDS; several PDSs were averaged (taking into account observation windows). The white noise level was subtracted from each averaged PDS leaving the rms fractional variability of the time series, and the powers were multiplied with the frequencies yielding  $\nu P_\nu$  prescription (i.e., integrated power in  $(\text{rms}/\text{mean})^2$ ; Belloni et al. (1997)). Our resulting PDSs for our sources are displayed in Figure 4. We do not find any effect of the orbital periods for any of our three sources (0.075–0.1 mHz) in the PDSs we calculate. This is an effect of our analysis method (stack-averaged PDS) and the fact that these periodicities are in the error range of the lowest frequency bin of our calculated PDSs. In addition, we do not have a contribution (i.e., periodicity) from the satellite (NuSTAR) orbital motion ( $\sim 0.17$  mHz) for the same reasons. Subsequently, we fitted the PDS with the analytical model  $\nu P(\nu) = P_2 \times (1 + (\nu/P_1)^4)^{-1/4}$  (where  $P_1$  is the break frequency  $\nu_0$ ) that is used to describe the PDS of sources with truncated accretion disks (Revnivtsev et al. 2010, 2011; Balman & Revnivtsev 2012; Balman 2015). Additional Lorentzian functions were introduced for adequate modeling of the PDS. The fits show frequency breaks in the PDS of our

<sup>12</sup> <https://heasarc.gsfc.nasa.gov/lheasoft/ftools/xronos.html>



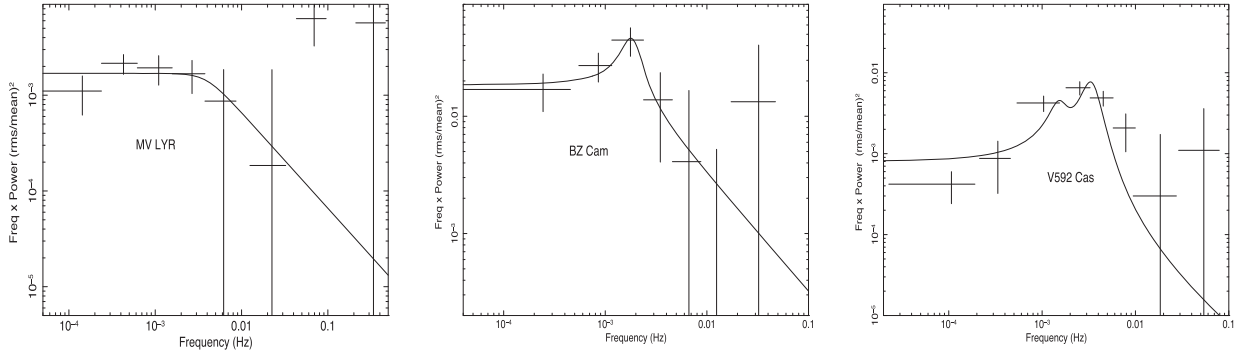


**Figure 4.** PDS of MV Lyr (for comparison), BZ Cam, and V592 Cas obtained using NuSTAR light curves. Overplotted are the fits for MV Lyr, BZ Cam, and V592 Cas (see the text for details). One Lorentzian for BZ Cam and two additional Lorentzian models for V592 Cas were used to achieve an adequate fit.

NLs as  $3.9 \pm 2.5$  mHz for MV Lyr,  $2.5 \pm 2.0$  mHz for BZ Cam, and  $<10$  mHz for V592 Cas (ranges for BZ Cam and MV Lyr correspond to a 90% confidence level and the  $\chi^2_\nu$  of the fits are 0.9–1.3). During the fitting procedure, one Lorentzian with a peak frequency at about  $1.7 \pm 0.7$  mHz was included for BZ Cam, which compensated for the peaked noise component; however, the significance of this component is only  $1\sigma$ . For V592 Cas, two Lorentzians were used to achieve a good fit. One of them is a QPO component (i.e., narrow,  $[\nu/\text{FWHM}] < 2$  van der Klis 2006) with a peak at  $1.4^{+2.6}_{-0.3}$  mHz and the other is a peaked noise component ( $[\nu/\text{FWHM}] > 2$ ) with  $3.6 \pm 0.4$  mHz (ranges of errors correspond to 90% confidence level). The narrow QPO component is detected in both the power spectrum with the Miyamoto normalization and its integrated power spectrum ( $\nu P_\nu$ ). Our assumed broken-power-law model was fitted together with the Lorentzians to find the break frequency. However, the fits were not sensitive to this component, and we derived an upper limit of  $<10$  mHz for V592 Cas. Our results show that the PDS structure of these three NLs resemble DNe PDSs and its variations between quiescence and high states, which will be elaborated in the next section.

## 5. Discussion

### 5.1. The Power Spectra

We have investigated the red noise structure in three NL sources (BZ Cam, V592 Cas, and MV Lyr for comparison) to reflect upon the advective hot flows independently from the spectral analysis, study their variability characteristics, and find their transition radii where the optically thick flow truncates in NL-type CVs. Propagating fluctuation models predict that a truncated optically thick accretion disk should lack some part of its aperiodic variability at high Fourier frequencies. The calculated PDSs show frequency breaks at  $3.9 \pm 2.5$  mHz for MV Lyr,  $2.5 \pm 2.0$  mHz for BZ Cam, and  $<10$  mHz for V592 Cas with a peaked noise component at  $1.7 \pm 0.7$  mHz for BZ Cam and  $3.6 \pm 0.4$  mHz for V592 Cas. Assuming the simple relation,  $\nu_0 = (1/2\pi)(GM_{\text{WD}}/R_{\text{in}}^3)^{1/2}$ , the frequency breaks correspond approximately to a transition/truncation radii at about  $R_{\text{tr}} \sim 5.5 \pm 2.0 \times 10^9$  cm for MV Lyr,  $\sim 7.4 \pm 2.4 \times 10^9$  cm for BZ Cam, and  $>3.0 \times 10^9$  cm for V592 Cas. This is a strong indication of extended structures for our NLs in the

X-ray regime. In addition, we have detected a QPO at  $1.4^{+2.6}_{-0.3}$  mHz for V592 Cas where an optical QPO had been detected previously, as well, at a lower frequency of about 0.75 mHz (Kato & Starkey 2002). Figure 4 displays the PDS of MV Lyr, BZ Cam, and V592 Cas with an increasing accretion rate from left to right. These three sources (NLs) are high-state CVs, but MV Lyr indicates a PDS more similar to quiescent DN at the low accretion limit of about  $10^{-9} M_\odot \text{ yr}^{-1}$  calculated from the UV/optical. As seen from the figure, increasing accretion rate shifts the noise toward higher frequencies, and in BZ Cam we see a peaked noise component most likely originating in the advective hot flow (increased variability in the hot flow). This peaked noise component originating from the hot flow perhaps becomes more coherent once the accretion rate surpasses  $10^{-8} M_\odot \text{ yr}^{-1}$  yielding the QPO structure we detect, and the peaked noise moves toward a higher frequency. It has been suggested that such a QPO may be associated with the break frequency or with the precession/oscillations of the inner hot flow (van der Klis 2006; Ingram & van der Klis 2013). We note that V592 Cas has a precessing disk with positive and negative superhumps (see Section 1.1). The PDS of V592 Cas resembles the PDS of SS Cyg at high state (during the optical peak) with a similar accretion rate (Schreiber & Lasota 2007); however the truncation radius is further out in the disk of V592 Cas by at least a factor of 3. As for the correspondence of PDS with other X-ray binaries, a long discussion has been made in Balman (2019) for general CVs and the changes of the noise structure with increasing accretion rate is observed in other X-ray binaries with noise shifting to higher frequencies and becoming more coherent (appearance of QPOs), and Lorentzian peaks are used to model the hard state or quiescent PDS of LMXBs where the advective hot flows dominate (the variability of) the accretion disk (Belloni 2010; Muñoz-Darias et al. 2014; Degenaar et al. 2018).

### 5.2. Characteristics of Advective Hot Flows

The X-ray emission from NLs and nonmagnetic CVs (and perhaps most AWBs) are adequately explained with radiatively inefficient advective hot accretion flows (RIAF ADAF-like) in the close vicinity of the WD (see Balman 2015, 2020, and references therein). We find that the RIAF ADAF-like accretion flows in nonmagnetic CVs are mainly thermal in X-rays with low or higher nonequilibrium ionization effects due to the nature of the flow, its

viscosity, and its turbulence. One of the basic properties of such flows is the radiative efficiency, which we calculate in this study within a wide energy band of 0.1–100 keV for both BZ Cam and V592 Cas. The spectral results in Tables 1 and 2 show a total X-ray luminosity of  $(1.1\text{--}1.6) \times 10^{32}$  erg s<sup>-1</sup> and  $(1.2\text{--}1.8) \times 10^{32}$  erg s<sup>-1</sup> for BZ Cam and V592 Cas, respectively. The accretion luminosities of these sources as calculated from the optical and UV wavelengths are  $\sim 3 \times 10^{34}$  erg s<sup>-1</sup> and  $\sim 1.2 \times 10^{35}$  erg s<sup>-1</sup> (V592 Cas; see Table 1 Balman et al. 2014, and references therein). As a result, the radiative efficiency ( $\epsilon = L_x/L_{\text{opt/UV}}$ ) in the X-ray emitting region is  $\sim 0.004\text{--}0.005$  for BZ Cam (an upper limit as  $L_{\text{opt/UV}}$  can be higher) and  $\sim 0.001\text{--}0.002$  for V592 Cas. These calculations of luminosities (i.e., larger than Swift results) and efficiencies (i.e., smaller than Swift results) are consistent, but are revised versions of the Swift spectral results presented in Balman et al. (2014). Therefore, the X-ray emission efficiency is about 0.1%–0.5% of the accretion luminosity of these sources.

The nonthermal power-law emission components detected in this study, have luminosities of  $(4.6\text{--}5.4) \times 10^{31}$  erg s<sup>-1</sup> (BZ Cam) and  $(0.9\text{--}1.1) \times 10^{32}$  erg s<sup>-1</sup> (V592 Cas) and are a factor of 2 larger for V592 Cas. Nonthermal (power law-type) X-ray emission is about 0.2% of the accretion luminosity for BZ Cam, and it is about 0.1% of the accretion luminosity of V592 Cas. In general, inefficiencies in the X-ray luminosities are consistent with expectations of radiatively inefficient advective hot flows (RIAF ADAF-like) in the X-ray emitting regions. The existence of low-luminosity power-law emission in the X-rays is justified as the accretion flow does not cool either thermally or via Compton cooling (i.e., marginal cooling). As the flow does not radiate and cool, the energy is carried within the flow and advected into the WD heating the WD or energy is channeled to aid formation of outflows from the disk in the X-ray emitting or other regions further out (see also Narayan & Yi 1995).

Narayan & McClintock (2008) and Yuan & Narayan (2014) review the characteristics of advective hot flows in several different regimes, mostly for black holes. One of the basic criteria is the efficiency factor, which is given with respect to the Eddington luminosity prescription as  $\epsilon = L/(\dot{M}_{\text{BH}}c^2)$ , where  $L$  is the source luminosity and the denominator represents the total accretion energy budget of the black hole. In the regime,  $\dot{M}/\dot{M}_{\text{Edd}} < 10^{-3}$  (depends on the square of the  $\alpha$  parameter), advection dominates the flow, and as the accretion rate increases, the fraction of advection in the flow drops and the flow becomes more radiative. Note that the fraction of advection is a function of  $r$  in the disk and the accretion rate, and the optically thick part of the disk flow can be sustained. This yields a two-zone accretion flow where there is a cool geometrically thin disk at large radii and a hot accretion flow at small radii (Done et al. 2007, and references therein). In addition, there is a TCAF model (two-component ADAF model) where the optically thick Keplerian disk is surrounded by a sub-Keplerian flow (halo) and a standing shock leads to an inner extended post-shock halo (Chakrabarti 1990; Chakrabarti & Titarchuk 1995).

At low  $\epsilon$  (efficiency) limit gas is heated but hardly cools (our NL sources resemble this). In this regime both electrons and ions are radiatively inefficient; electrons are unable to radiate the viscous heat they acquire, and the Coulomb collisions are inefficient for heat transfer. Note here that radiative cooling depends on gas density; thus this is also low. As  $\dot{M}$  increases,  $\epsilon$

also increases and electrons start radiating the viscous energy they attain and part of the energy they obtain from ions (Yuan & Narayan 2014). These types of advective hot flows (RIAF ADAF-like) at relatively lower accretion rates compared to  $\dot{M}_{\text{Edd}}$  are expected to be in nonequilibrium ionization creating 2-T flow structure. As a result, the existence of a NEI flow structure is a typical characteristic, and we recover this for both of the NL sources in our study. Furthermore, Comptonization of the flow depends strongly on the accretion rate and is expected to be a weak component at low accretion rates and at low radiative efficiencies compared to Eddington values. The power-law components of BZ Cam and V592 Cas (2 times stronger than BZ Cam in luminosity) are only 0.1–0.2% of their accretion luminosity, which is consistent with these expectations. Moreover, in ADAF flows at radii where the gas is cool enough, heavier atomic species iron peak elements can retain electrons and show emission lines (Narayan & Raymond 1999). Note here that RIAF ADAF flows are virialized with expected temperatures of MeV in BH or NS compact binaries, but the X-ray emission is detected at temperatures around 100 keV or less owing to a 2-T regime between electrons and ions and/or several cooling mechanisms that exist in different hot flow regimes (Yuan & Narayan 2014). However, the virial temperatures in AWBs (i.e., for CVs) are 10–45 keV (Balman et al. 2014; Balman 2020), and the observed X-ray temperatures are consistent with virial temperatures; therefore the flows are already virialized. On the other hand, the X-ray temperatures of the two NLs in this study are somewhat lower due to the NEI characteristics of the flow (fitted models reflect the electron temperatures). We stress here that ADAF flows that represent a 2-T flow may be approximated with a single T (flow may mimic single T) as these are not the type of 2-T flows around BHs as they are in a shallower gravitational potential well with no general relativistic effects. However, effects of turbulence due to magnetic effects (i.e., Alfvénic waves) and magnetorotational-instability-related (MRI) turbulence should also be considered for advective hot flows. In general, magnetic turbulence promotes disequilibrium between electrons and ions. When the magnetic energy density is greater than the thermal energy density in the flow, electrons are preferentially heated, whereas in the opposite case, ions are heated (Howes 2010; Kawazura et al. 2019, and references therein). Even at a constant magnetic field in the flow, turbulent heating would gradually increase the thermal to magnetic energy ratio of ions to a state of dominant ion heating. Thus, existing magnetic fields and turbulence are capable of pushing a weakly collisional plasma system away from thermal equilibrium.

Recently, Datta et al. (2021) have performed calculations of shock formation in ADAF flows around accreting WDs. For a transonic flow around an accretor with a hard surface (i.e., WD or NS) shocks are to occur given some boundary conditions and system parameters as the flow has to slow down at the surface (Dhang et al. 2016). The formation of shocks enhances in a transonic sub-Keplerian flow once inner and outer critical points coexist (Chakrabarti 1996). Datta et al. (2021) solved the hydrodynamical problem between these critical points to see when the shock conditions are satisfied and find that for a WD of mass  $0.8M_{\odot}$  and  $0.01R_{\odot}$ , and for other given system parameters like rotation and eccentricity, a shock occurs around  $1.3 \times 10^9$  cm, which is very close to the WD. Shocks in general will enhance densities; hence Coulomb collisions and emissivity thus also enhance radiative efficiency. The formation of

shocks in the advective hot flows can be articulated in the context of all AWBs. Given Section 2.3 of Balman (2020), the advective hot flows in quiescent dwarf nova mimic CIE flows with near-solar abundances and inefficiency in line emissivity. DNe in quiescence show optically thick disk flow truncation of radii  $(3\text{--}10) \times 10^9$  cm (Balman & Revnivtsev 2012), which yields enough distance for acceleration of the transonic advective hot flow and formation of shocks near the WD (see also Datta et al. 2021). This will yield enhancement of X-ray emission (increase of efficiency) in a small zone near the WD, which can also explain some of the detected eclipse-like effects at high inclinations (rather nondetections at low count rates) in quiescent DNe. The existence of shocks can be effective in NLs, as well.

### 5.3. Iron Emission and Absorption Lines

The emission lines incorporated in Fit-2 of both sources are designated iron ionization emission lines of He-like (Fe XXV) and H-like (Fe XXVI) species expected from the thermal plasma along with the assumed Bremsstrahlung continuum. These lines are detected for BZ Cam at around 6.88–6.91 keV (H-like) and 6.52–6.57 keV (He-like) indicating a NEI nature for the accretion flow in the X-ray emitting region (ranges correspond to a 90% confidence level). V592 Cas shows dominantly the He-like emission line (complex) at around 6.56–6.66 keV. The H-like ionization line is included for completeness and detected at  $1\sigma$  significance around 6.84–6.96 keV where the energy ranges and dominance of the He-line (absence of the H-like line) support the NEI nature. As the plasma in these NLs is not in equilibrium, the line centroids from the under-ionized plasma do not appear at their equilibrium values (6.97 keV for the H-like and the 6.7 keV for the He-like iron emission lines), and they are detected at slightly lower energies. As a result, the Gaussian emission lines used for Fit-2 on Tables 1 and 2 reveal NEI conditions on the lines and the plasma, so Fit-2 and Fit-1 (NEI model fits) confirm each other explicitly. Note that the He-like line is a blended triplet line feature that is composed of the resonance, intercombination and the forbidden line emission components (due to inadequate spectral resolution). The NEI conditions imply shifts to lower energies from the equilibrium line centers as a result of the fact that the forbidden line emission is enhanced in the triplet emission. Given the low hydrogen column densities derived from the fits for both NLs, if the iron line emission was due to photoionization, the resonance line should have dominated the He-line complex and this is not what we observe (see Bianchi et al. 2005). The range of ionization timescales is  $(2.0\text{--}9.0) \times 10^{11}$  s  $\text{cm}^{-3}$  (within a 90% confidence level) where these values indicate that the plasma is not in equilibrium as the timescales would then exceed several times  $10^{12}$  s  $\text{cm}^{-3}$  (Liedahl 1999). We note also that a study published on the archival Chandra HETGS data of CVs by Schlegel et al. (2014) indicate line emission consistent with multitemperature plasma in a nonequilibrium state with  $n_e$  between  $10^{12}\text{--}10^{16}$   $\text{cm}^{-3}$  that can be attributed to characteristics of advective hot flows.

In order to reduce the residual fluctuations around the iron line complex, further modeling showed an absorption line around 7.00–7.13 keV for BZ Cam and 6.94–7.05 keV for V592 Cas with significant widths (see 3). These absorption lines indicate optical depths at the line centers of 1.13–0.7 for V592 Cas (i.e., optically thin flow), but for BZ Cam the ranges

change from 4.6–11.6 to 35–62 depending on the model fit. We believe the inconsistency for BZ Cam is a result of the P Cygni structure on the line shape, on which we will elaborate in the following paragraph. Such iron absorption lines are indicators of warm absorbers and thus, their detection suggests existence of warm absorption in both of the NLs similar to X-ray binaries (Balman 2009; Díaz Trigo & Boirin 2016). Both of our sources have substantial wind outflows and existence of extended structure in the UV/optical wavelengths (see 1 and Section 4 in Balman 2020). Note that the iron absorption line ranges are close to or include the iron K-edge absorption around 7.11 keV; however the X-ray spectra and temperatures detected in these two NLs do not adequately support such a scenario for a fully ionized hot accretion disk coronae.

These iron absorption line features along with the emission lines at the same energies as the H-like species can be a result of P Cygni profiles in the X-rays for the H-like iron emission line. This shows existence of outflows from the X-ray emitting plasma. The outflow speeds can be inferred from the difference between the emission peak and the absorption dip energies using the fits in Tables 1 and 2. This has been readily tested for BZ Cam as the H-like iron line emission is securely detected ( $3\sigma\text{--}4\sigma$ ). Both of Fit-2 (also tested with Fit-1) are performed without the emission and absorption lines around the H-like iron line energies. Figure 5 shows the P Cygni-type variation in the residuals for BZ Cam when these two features are removed from Fit-2 with a power-law component (everything else remains; the He-like iron and the 6.4 keV reflection line is fitted). The difference in the emission and absorption line centroids (GAUSS and GABS models) in Fit-2 of BZ Cam yield speeds (using the Doppler formula) of  $0.029c\text{--}0.015c$  that corresponds to  $4500\text{--}8700$   $\text{km s}^{-1}$  including the error range of the centroid parameters. This is the first time we recover a jet-like outflow in the X-rays from an accreting CV. The wind speed in BZ Cam ranges in  $3000\text{--}5300$   $\text{km s}^{-1}$ ; thus the broadband X-ray spectrum reveals similar or larger outflow speeds as they are produced deeper in the potential well where the inner advective hot flow dominates. Note that Figure 5 includes a fit to V592 Cas spectra (using Fit-2 in Table 2) produced in the same manner, excluding the He-like iron line, as well, for comparison. The existence of a P Cygni-type variation cannot be properly confirmed on any H-like iron line. The figure mostly indicates the significance of the Fe XXV (He-like iron) and the H-like iron absorption line ( $\sim 3\sigma$ ). Such characteristic outflows as in BZ Cam (for that matter in V592 Cas assuming optical and UV) have been observed in AGNs and XRBs as disk-driven winds (Elvis 2000), thermally driven winds emanating from the dusty torus of AGNs (Krolik & Kriss 2001) and as part of the hot accretion flows and their outflows modeled with MHD/GRMHD (see Yuan & Narayan 2014, for a review). The blueshifted iron K-shell lines in radio-quiet AGN have been interpreted with ultrafast outflows (UFO) defined as highly ionized winds (ionization parameter  $\log(\xi)$  3–6) outflowing at velocities in excess of  $10,000$   $\text{km s}^{-1}$  (Tombesi et al. 2010). Thus, UFOs are disk-winds close to the black holes, whereas the warm absorbing disk-winds in AGNs and XRBs are slower at  $300\text{--}4000$   $\text{km s}^{-1}$  and produced further out forming a stratified wind (Ponti et al. 2012; Díaz Trigo & Boirin 2016, and references therein). These winds can carry significant amount of mass comparable or even larger than the amount of accreted material (e.g., Degenaar et al. 2014).

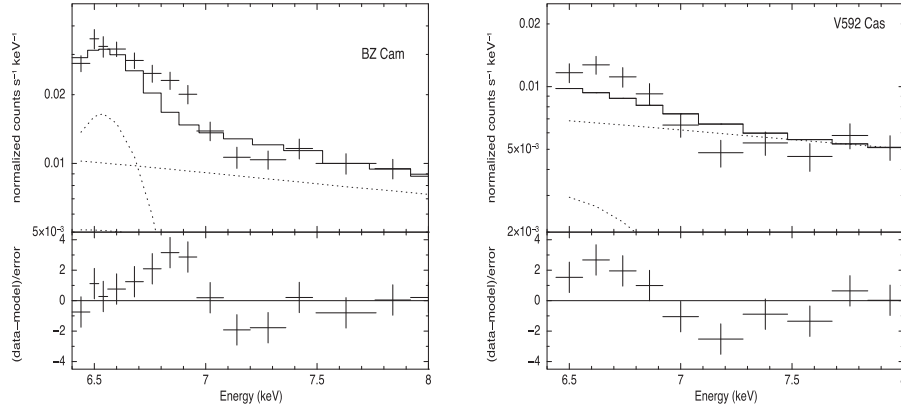


**Figure 5.** Variation around the H-like iron line for BZ Cam on the left and V592 Cas on the right. The fitted spectrum of BZ Cam using model Fit-2 in Table 1 is displayed where only the H-like iron emission line and the absorption feature in this energy are excluded from the fitting process. Note the P Cygni-type variation in the residuals (lower panel) around the expected ionization line centroid 6.97 keV. On the right are the deviations in sigmas (residuals) produced using Fit-2 for V592 Cas in the same manner as with BZ Cam along with an additional exclusion of the He-like iron emission line for V592 Cas. The figure mostly indicates the significance of the He-like iron emission line and the H-like absorption line. No P Cygni-type variation as in BZ Cam is observed.

The outflow of BZ Cam detected in the X-ray regime can also help explain the existing bow-shock nebula and the mass associated with it (see 1). The bow-shock nebula around BZ CM is claimed to be of several recurrent novae that occurred in the system with timescales of millennia (Hoffmann & Vogt 2020) indicating 3–4 shells assuming nova expansion velocities (the detected curvature radii of the shells around the source are  $16''$ – $61''$ , which are less than 0.1 pc at the GAIA distance of BZ Cam). There are prominent OIII and H $\alpha$  emission structures associated with this bow-shock nebula (or the nova shells; Bond & Miszalski 2018). Tappert et al. (2020) found an H $\alpha$  luminosity of  $5.1 \times 10^{30}$  erg s $^{-1}$  and OIII luminosity of  $9.1 \times 10^{30}$  erg s $^{-1}$  where these luminosities overlap within errors. Such a bow-shock like nebula exists around the black hole binary Cyg X-1 (at relatively larger size, but concentric ring-like emission regions trailing the shock region (as in BZ Cam) are not detected). It is calculated that this bow-shock nebula is powered by the relativistic jet interaction with the circumstellar medium (see Russell et al. 2007, and references therein). There are prominent OIII and H $\alpha$  emission structures associated with this nebula with luminosities of  $(1.3\text{--}21) \times 10^{34}$  erg s $^{-1}$  and  $(1.8\text{--}25) \times 10^{34}$  erg s $^{-1}$  in OIII and H $\alpha$ , respectively. These luminosities match within errors and are calculated to be a result of a jet power of  $(4\text{--}14) \times 10^{36}$  erg s $^{-1}$  from the binary with X-ray luminosity of about  $1 \times 10^{37}$  erg s $^{-1}$ . The nebular luminosities (OIII and H $\alpha$ ) of the BZ Cam Nebula are about  $10^5$  less than Cyg X-1 and the source X-ray luminosities are less by about the same factor  $10^5$ . Thus, a jet-like collimated fast outflow that could power the BZ Cam bow-shock nebula (with a shock that will mimic a nova shell interaction) should have several times  $10^{31}$  erg s $^{-1}$  in the X-rays scaling from the jet power in Cyg X-1 nebular interaction. Such X-ray luminosities are well within the detected values in our study and available in the accretion flow as it is radiatively inefficient, and most of the accretion energy ( $\sim 1 \times 10^{34}$  erg s $^{-1}$ ) is carried in the flow (very low efficiency of emission in the X-ray region). Therefore, we suggest that the jet-like outflow detected in this study may create and/or power the bow-shock nebula of BZ Cam. The several ring-like structures may possibly be a result of turning

on and off of the jet-like outflow, or the enhancement in matter ejection of the jet-like outflow within several hundred years timescale. Assuming the mass-loss rate in the jet-like outflow is 0.01% of the accretion rate ( $5 \times 10^{-9} M_{\odot}$  yr $^{-1}$ ), for a timescale of  $10^6$ – $10^7$  yrs ( $\sim 100$  times less than CV evolution timescales), this will gather  $(5\text{--}50) \times 10^{-5} M_{\odot}$  mass in the circumstellar medium of BZ Cam, which is consistent with standard classical nova ejecta masses (Balman 2020) that could mimic a nova remnant and its interaction.

The P Cygni-type profile of the H-like iron line of BZ Cam indicates that we are looking into the outflow, where perhaps the nondetection of such a structure in V592 Cas may mean that the outflow is there, but not directed toward our line of sight. The error range of the centroid of the detected H-like absorption line for V592 Cas is consistent with blueshifts (in absorption), that is, a result of about  $3000$  km s $^{-1}$  outflows (using Fit-2) in accordance with the bipolar winds in this system. Thus, existence of a jet-like outflow from V592 Cas is not justified.

## 6. Summary

In this paper, we have presented the analysis of the broadband spectra of two NL systems, BZ Cam and V592 Cas, using the ROSAT, Swift, and NuSTAR observatory archival data together with the power spectral analysis of the NuSTAR data. We have considered the nature of the accretion flow and outflows in these systems as observed in the X-ray regime. We show that these objects have a hard X-ray spectrum over the 0.1–78 keV energy range with no soft (blackbody model) X-ray emission. We find that the X-ray energy spectral and power spectral characteristics reveal radiatively inefficient advective hot accretion flows (RIAF ADAF-like) in these two systems. Fits with multitemperature CIE model yield non-physical flat power-law indices showing marginal cooling and emission in the X-ray emitting region. We find X-ray luminosities of  $(1.1\text{--}1.6) \times 10^{32}$  erg s $^{-1}$  and  $(1.2\text{--}1.8) \times 10^{32}$  erg s $^{-1}$  for BZ Cam and V592 Cas, respectively. The radiative efficiencies for the NLs are about 0.004–0.005 for BZ Cam and 0.002–0.001 for V592 Cas comparing their X-ray luminosity with the accretion luminosity observed in the optical and UV.

As expected from the RIAF ADAF-type flows, we detect also nonthermal power-law emission components with a range of photon indices 1.76–1.87 ( $5 \times 10^{31} \text{ erg s}^{-1}$ ) for BZ Cam and 1.5–1.8 ( $9 \times 10^{31} \text{ erg s}^{-1}$ ) for V592 Cas. This component is expected to be low at low radiative efficiency and increase with the accretion rate. We find that this is only about (0.1–0.2)% of the accretion luminosity of the sources and that the power-law component increases with the accretion rate, as the power-law luminosity is twice as high in V592 Cas. In general, thermal X-rays are mainly from the vicinity of the WD originating from a radiatively inefficient hot accretion flow with NEI conditions. The nonthermal emission can be of the Comptonized part of the flow emission, and/or inverse Comptonized soft disk photons (e.g., corona), and/or originating from scatterings off the structures in the system (e.g., bipolar winds, disk itself) or perhaps originates in the jet-like outflow itself as in BZ Cam.

We recover a complex iron line structure in 6.0–7.0 keV. We detect the Fe XXV and Fe XXVI ionization emission lines except for the H-like iron from V592 Cas. None of the line centroids are found at their equilibrium values for both sources even using a free-free continuum, but they are found at slightly lower energies expected from plasma in NEI, which is characteristic of advective hot flows. In addition, we note that the He-like iron is a blend of the forbidden, intercombination, and resonance lines, and the shifts of centroids toward lower energies would be toward the forbidden emission line, which justifies the NEI conditions. Tables 1 and 2 reveal that NEI model fits yield a physically better description of the data with good  $\chi^2_\nu$  values at higher confidence levels in comparison to the rest of the models. We suggest that the detected radiatively inefficient advective hot flows portray a weakly collisional plasma in both NLs where magnetic turbulence effects (as a result of magnetorotational instabilities or Alfvénic waves) drive the plasma away from equipartition as the ions and electrons are heated differently.

The PDSs we calculate for the two NL sources (for BZ Cam at  $1\sigma$  only) show a peaked noise continuum component most likely originating from the hot flow. We find transitions of the optically thick flow into the inner advective hot flow at radii around  $R_{\text{tr}} \sim 7.4 \pm 2.4 \times 10^9 \text{ cm}$  for BZ Cam,  $5.5 \pm 2.0 \times 10^9 \text{ cm}$  for MV Lyr, and  $>3.0 \times 10^9 \text{ cm}$  for V592 Cas, where we also detect a QPO from this system (V592 Cas). All is in line with expectations from the X-ray binary sources (NS or BH) as their accretion rate increases the noise in the PDS shifts to higher frequencies and become more coherent. We find that the PDS of our NL sources are consistent with the DNe PDSs calculated in other studies in quiescence and in high state (NLs are high-state CVs). All fits show the existence of a 6.4 keV (6.2–6.5 keV) iron reflection line (with a width of 0.2–0.4 keV), which indicates the existence of a reflection spectrum or rather existence of reflection effects on the spectrum of both of the sources, but we do not detect the Compton reflection hump around 20–30 keV. Modeling the spectrum with available reflection models does not improve the fits (even when the power-law components are removed).

Finally, we detect H-like iron absorption lines (Fe XXVI) in both of the sources that yield large blueshifts. For BZ Cam we detect a P Cygni-type profile for the H-like iron owing to its shape in emission and absorption. A simple Doppler calculation yields outflow velocities of (4500–8700)  $\text{km s}^{-1}$ , and the outflow is directed toward the observer (i.e., jet-like outflow). This is the first time a jet-like outflow is detected in the X-rays from an accreting CV. We suggest that the bow-shock nebula around BZ Cam may be powered by the fast collimated outflow

from the binary (jet power  $\sim$ several  $\times 10^{31} \text{ erg s}^{-1}$ ), and the interaction and associated mass can mimic a classical nova remnant. BZ Cam possibly dissipates most of the gravitational power in the X-ray emitting region via jet-like outflows as a result of the radiatively inefficient advective accretion detected in the X-rays. The same H-like iron absorption in V592 Cas has no significant H-like emission line in the same range; thus it is possible that even if there is an outflow in the X-rays, it is not directed toward the observer. The absorption feature of V592 Cas yields blueshifts out to  $3000 \text{ km s}^{-1}$  consistent with the wind velocities detected in the optical and UV. The detected Fe XXVI absorption features indicate existence of warm absorber effects in both BZ Cam and V592 Cas as observed in the X-ray binaries. These two NL systems set an example of the characteristics of accretion in high state CVs with bipolar fast wind outflows as observed in the optical and UV. Their X-ray characteristics shed light on the theory of accretion in high-accretion-rate white dwarf binaries, as they portray the existence of radiatively inefficient advective hot flows with extended geometries and magnetically aided accretion and outflows, revealing a consensus of accretion physics around compact objects.

The authors acknowledge the NuSTAR Observatory for performing the observations of BZ Cam, V592 Cas, and MV Lyr. This work was partially supported by the Vaughan Family fund at University of Texas-San Antonio (UTSA). The authors thank Valery Suleimanov and Tomaso Belloni for comments on the manuscript and an anonymous referee for critical reading of the manuscript. S.B. thanks E. Sion, P. Szkody, D. Bisikalo, and R. Gonzalez-Riestra for helpful discussions and support with the NuSTAR proposal. P.G. is pleased to thank William P. Blair at the Henry A. Rowland Department of Physics and Astronomy, Johns Hopkins University, Baltimore, Maryland, for his kind hospitality. The results reported in this article are based on observations obtained with NuSTAR, Swift, and ROSAT. Swift is a NASA mission with participation of the Italian Space Agency and the UK Space Agency. The NuSTAR mission is a project led by the California Institute of Technology, managed by the Jet Propulsion Laboratory, and funded by the National Aeronautics and Space Administration. The ROSAT Project is supported by the Bundesministerium für Bildung, Wissenschaft, Forschung und Technologie (BMF/DLR), and the Max-Planck-Gesellschaft (MPG). This research has made use of the NuSTAR Data Analysis Software (NuSTARDAS) jointly developed by the ASI Science Data Center (ASDC, Italy) and the California Institute of Technology (USA). It has also made use of the XRT Data Analysis Software (XRTDAS) developed under the responsibility of the ASI Science Data Center (ASDC), Italy. This research has made use of data and/or software provided by the High Energy Astrophysics Science Archive Research Center (HEASARC), which is a service of the Astrophysics Science Division at NASA/GSFC.

## ORCID iDs

Şölen Balman  <https://orcid.org/0000-0001-6135-1144>  
 Eric M. Schlegel  <https://orcid.org/0000-0002-4162-8190>  
 Patrick Godon  <https://orcid.org/0000-0002-4806-5319>

## References

- Arnaud, K. A. 1996, in ASP Conf. Ser. 101, *Astronomical Data Analysis Software and Systems V*, ed. G. H. Jacoby & J. Barnes (San Francisco, CA: ASP), 17

- Balman, Ş. 2009, *AJ*, **138**, 50
- Balman, S. 2015, in *Acta Polytechnica CTU Proc.* 2 ed. F. Giovannelli & L. Sabau-Graziati (Prague: CTU), 116
- Balman, Ş. 2019, *AN*, **340**, 296
- Balman, Ş. 2020, *AdSpr*, **66**, 1097
- Balman, Ş., Godon, P., & Sion, E. M. 2014, *ApJ*, **794**, 84
- Balman, Ş., Godon, P., Sion, E. M., et al. 2011, *ApJ*, **741**, 84
- Balman, Ş., & Revnivtsev, M. 2012, *A&A*, **546**, A112
- Baptista, R. 2016, in *Astronomy at High Angular Resolution*, ed. H. M. J. Boffin, 439 (Cham: Springer), 155
- Belloni, T., & Hasinger, G. 1990, *A&A*, **230**, 103
- Belloni, T. M. 2010, in *The Jet Paradigm, Lecture Notes in Physics*, ed. T. Belloni, 794 (Berlin: Springer), 53
- Belloni, T., van der Klis, M., Lewin, W. H. G., et al. 1997, *A&A*, **322**, 857
- Bianchi, S., Matt, G., Nicastro, F., Porquet, D., & Dubau, J. 2005, *MNRAS*, **357**, 599
- Bond, H. E., & Miszalski, B. 2018, *PASP*, **130**, 094201
- Bruch, A. 2015, *A&A*, **579**, A50
- Burrows, D. N., Hill, J. E., Nousek, J. A., et al. 2005, *SSRv*, **120**, 165
- Chakrabarti, S., & Titarchuk, L. G. 1995, *ApJ*, **455**, 623
- Chakrabarti, S. K. 1990, *MNRAS*, **243**, 610
- Chakrabarti, S. K. 1996, *PhR*, **266**, 229
- Churazov, E., Gilfanov, M., & Revnivtsev, M. 2001, *MNRAS*, **321**, 759
- Datta, S. R., Dhang, P., & Mishra, B. 2021, *ApJ*, **918**, 87
- Degenaar, N., Ballantyne, D. R., Belloni, T., et al. 2018, *SSRv*, **214**, 15
- Degenaar, N., Maitra, D., Cackett, E. M., et al. 2014, *ApJ*, **784**, 122
- Dhang, P., Sharma, P., & Mukhopadhyay, B. 2016, *MNRAS*, **461**, 2426
- Díaz Trigo, M., & Boirin, L. 2016, *AN*, **337**, 368
- Dobrotka, A., Mineshige, S., & Casares, J. 2012, *MNRAS*, **420**, 2467
- Dobrotka, A., Ness, J. U., & Bajčičáková, I. 2016, *MNRAS*, **460**, 458
- Dobrotka, A., Ness, J. U., Mineshige, S., & Nucita, A. A. 2017, *MNRAS*, **468**, 1183
- Done, C., Gierliński, M., & Kubota, A. 2007, *A&ARv*, **15**, 1
- Elvis, M. 2000, *ApJ*, **545**, 63
- Gilfanov, M. 2010, in *The Jet Paradigm, Lecture Notes in Physics*, ed. T. Belloni, 794 (Berlin: Springer), 17
- Gilfanov, M., & Arefiev, V. 2005, arXiv:astro-ph/0501215
- Godon, P., Regev, O., & Shaviv, G. 1995, *MNRAS*, **275**, 1093
- Godon, P., & Sion, E. M. 2003, *ApJ*, **586**, 427
- Godon, P., Sion, E. M., Balman, Ş., & Blair, W. P. 2017, *ApJ*, **846**, 52
- Greiner, J., Tovmassian, G., Orío, M., et al. 2001, *A&A*, **376**, 1031
- Griffith, D., Fabian, D., & Sion, E. M. 1995, *PASP*, **107**, 856
- Harrison, F. A., Craig, W. W., Christensen, F. E., et al. 2013, *ApJ*, **770**, 103
- Hertfelder, M., & Kley, W. 2015, *A&A*, **579**, A54
- Hertfelder, M., & Kley, W. 2017, *A&A*, **605**, A24
- Hoard, D. W., Kafka, S., Wachter, S., et al. 2009, *ApJ*, **693**, 236
- Hoffmann, S. M., & Vogt, N. 2020, *MNRAS*, **497**, 1419
- Honeycutt, R. K., Kafka, S., & Robertson, J. W. 2013, *AJ*, **145**, 45
- Howes, G. G. 2010, *MNRAS*, **409**, L104
- Hubeny, I., & Long, K. S. 2021, *MNRAS*, **503**, 5534
- Huber, M. E., Howell, S. B., Ciardi, D. R., & Fried, R. 1998, *PASP*, **110**, 784
- Ingram, A., & Done, C. 2011, *MNRAS*, **415**, 2323
- Ingram, A., & van der Klis, M. 2013, *MNRAS*, **434**, 1476
- Ingram, A. R. 2016, *AN*, **337**, 385
- Kafka, S., Hoard, D. W., Honeycutt, R. K., & Deliyannis, C. P. 2009, *AJ*, **137**, 197
- Kafka, S., & Honeycutt, R. K. 2004, *AJ*, **128**, 2420
- Kato, T., & Starkey, D. R. 2002, *IBVS*, **5358**, 1
- Kawazura, Y., Barnes, M., & Schekochihin, A. A. 2019, *PNAS*, **116**, 771
- Kimura, M., Yamada, S., Nakaniwa, N., et al. 2021, *PASJ*, **73**, 1262
- Kinch, B. E., Schnittman, J. D., Kallman, T. R., & Krolik, J. H. 2016, *ApJ*, **826**, 52
- Krautter, J., Klaas, U., & Radons, G. 1987, *A&A*, **181**, 373
- Krolik, J. H., & Kriss, G. A. 2001, *ApJ*, **561**, 684
- Kuulkers, E., Norton, A., Schwope, A., & Warner, B. 2006, in *Compact Stellar X-Ray Sources*, ed. W. Lewin & M. van der Klis, 39 (Cambridge: Cambridge Univ. Press), 421
- Lasota, J. P. 2004, in *IAU Coll. 194, Compact Binaries in the Galaxy and Beyond*, ed. E. Sion & G. Tovmassian, 124
- Liedahl, D. A. 1999, in *X-Ray Spectroscopy in Astrophysics, Lecture Notes in Physics*, ed. J. van Paradijs & J. A. M. Bleeker, 520 (Berlin: Springer), 189
- Liedahl, D. A., Osterheld, A. L., & Goldstein, W. H. 1995, *ApJL*, **438**, L115
- Linnell, A. P., Godon, P., Hubeny, I., Sion, E. M., & Szkody, P. 2010, *ApJ*, **719**, 271
- Long, K. S., & Knigge, C. 2002, *ApJ*, **579**, 725
- Lynden-Bell, D., & Pringle, J. E. 1974, *MNRAS*, **168**, 603
- Lyubarskii, Y. E. 1997, *MNRAS*, **292**, 679
- Mauche, C. W., & Mukai, K. 2002, *ApJL*, **566**, L33
- Mereghetti, S., Balman, S., Caballero-Garcia, M., et al. 2021, *ExA*, **52**, 309
- Meyer, F., & Meyer-Hofmeister, E. 1994, *A&A*, **288**, 175
- Miyamoto, S., Kimura, K., Kitamoto, S., Dotani, T., & Ebisawa, K. 1991, *ApJ*, **383**, 784
- Muñoz-Darias, T., Fender, R. P., Motta, S. E., & Belloni, T. M. 2014, *MNRAS*, **443**, 3270
- Narayan, R., & McClintock, J. E. 2008, *NewAR*, **51**, 733
- Narayan, R., & Popham, R. 1993, *Natur*, **362**, 820
- Narayan, R., & Raymond, J. 1999, *ApJL*, **515**, L69
- Narayan, R., & Yi, I. 1995, *ApJ*, **444**, 231
- Page, K. L., Osborne, J. P., Beardmore, A. P., et al. 2014, *A&A*, **570**, A37
- Pandel, D., Córdova, F. A., Mason, K. O., & Priedhorsky, W. C. 2005, *ApJ*, **626**, 396
- Patterson, J., Patino, R., Thorstensen, J. R., et al. 1996, *AJ*, **111**, 2422
- Patterson, J., & Raymond, J. C. 1985, *ApJ*, **292**, 535
- Ponti, G., Fender, R. P., Begelman, M. C., et al. 2012, *MNRAS*, **422**, L11
- Popham, R. 1999, *MNRAS*, **308**, 979
- Popham, R., & Narayan, R. 1995, *ApJ*, **442**, 337
- Pratt, G. W., Mukai, K., Hassall, B. J. M., Naylor, T., & Wood, J. H. 2004, *MNRAS*, **348**, L49
- Prinja, R. K., Knigge, C., Witherick, D. K., Long, K. S., & Brammer, G. 2004, *MNRAS*, **355**, 137
- Puebla, R. E., Diaz, M. P., Hillier, D. J., & Hubeny, I. 2011, *ApJ*, **736**, 17
- Puebla, R. E., Diaz, M. P., & Hubeny, I. 2007, *AJ*, **134**, 1923
- Revnivtsev, M., Burenin, R., Bikmaev, I., et al. 2010, *A&A*, **513**, A63
- Revnivtsev, M., Churazov, E., Postnov, K., & Tsygankov, S. 2009, *A&A*, **507**, 1211
- Revnivtsev, M., Potter, S., Kniazev, A., et al. 2011, *MNRAS*, **411**, 1317
- Ringwald, F. A., & Naylor, T. 1998, *AJ*, **115**, 286
- Ross, R. R., & Fabian, A. C. 2005, *MNRAS*, **358**, 211
- Russell, D. M., Fender, R. P., Gallo, E., & Kaiser, C. R. 2007, *MNRAS*, **376**, 1341
- Scaringi, S., Körding, E., Groot, P. J., et al. 2013, *MNRAS*, **431**, 2535
- Scaringi, S., Körding, E., Uttley, P., et al. 2012, *MNRAS*, **427**, 3396
- Schlegel, E. M., Shipley, H. V., Rana, V. R., Barrett, P. E., & Singh, K. P. 2014, *ApJ*, **797**, 38
- Schreiber, M. R., & Lasota, J. P. 2007, *A&A*, **473**, 897
- Semena, A. N., Revnivtsev, M. G., Buckley, D., Lutovinov, A. A., & Breitenbach, H. 2016, *AstL*, **42**, 379
- Shakura, N. I., & Sunyaev, R. A. 1973, *A&A*, **500**, 33
- Singh, K. P., White, N. E., & Drake, S. A. 1996, *ApJ*, **456**, 766
- Sion, E. M. 1985, *ApJ*, **292**, 601
- Stehle, R., & King, A. R. 1999, *MNRAS*, **304**, 698
- Suleimanov, V., Hertfelder, M., Werner, K., & Kley, W. 2014, *A&A*, **571**, A55
- Tappert, C., Vogt, N., Ederocliffe, A., et al. 2020, *A&A*, **641**, A122
- Taylor, C. J., Thorstensen, J. R., Patterson, J., et al. 1998, *PASP*, **110**, 1148
- Tombesi, F., Sambruna, R. M., Reeves, J. N., et al. 2010, *ApJ*, **719**, 700
- Uttley, P., Wilkinson, T., Cassatella, P., et al. 2011, *MNRAS*, **414**, L60
- van der Klis, M. 2006, *Compact Stellar X-ray Sources*, 39 (Cambridge: Cambridge Univ. Press), 39
- van Teeseling, A., Beuermann, K., & Verbunt, F. 1996, *A&A*, **315**, 467
- Wada, Q., Tsujimoto, M., Ebisawa, K., & Hayashi, T. 2017, *PASJ*, **69**, 10
- Warner, B. 1995, *Compact Astrophysics Series*, 28 (Cambridge: Cambridge Univ. Press)
- Wilms, J., Allen, A., & McCray, R. 2000, *ApJ*, **542**, 914
- Yuan, F., & Narayan, R. 2014, *ARA&A*, **52**, 529
- Zemko, P., Orío, M., Mukai, K., & Shugarov, S. 2014, *MNRAS*, **445**, 869